RESEARCH ARTICLE
SOLID EARTH: GEOMAGNETISM

Earth and Planetary Physics
9: 550–563, 2025
doi: 10.26464/epp2025029

A multisource geomagnetic field model incorporating ocean circulation-induced magnetic field

HongBo Yao[1], JuYuan Xu[1], Cong Yang[2], ZhengYong Ren[2], and Keke Zhang[1*]

[1]Macau Institute of Space Technology and Application, Macau University of Science and Technology, Macao 999078, China;

[2]School of Geosciences and Info-Physics, Central South University, Changsha 410083, China

Key Points:

- We introduce a method to incorporate the magnetic field induced by ocean circulation into geomagnetic field modeling.
- We show that neglecting the ocean circulation-induced magnetic field in geomagnetic field modeling results in leakage into the core field model.
- A new multisource geomagnetic field model (MGFM) is derived using over 20 years of magnetic data from MSS-1, *Swarm*, CryoSat-2, and CHAMP satellites.

Citation: Yao, H. B., Xu, J. Y., Yang, C., Ren, Z. Y., and Zhang, K. (2025). A multisource geomagnetic field model incorporating ocean circulation-induced magnetic field. *Earth Planet. Phys.*, *9*(3), 550–563. http://doi.org/10.26464/epp2025029

Abstract: The movement of global ocean circulation in the Earth's main magnetic field generates a measurable induced magnetic field (about 2 nT at geomagnetic satellite altitudes). However, this ocean circulation-induced magnetic field has not been previously estimated or incorporated into geomagnetic field models, potentially causing leakage into the core field model. Here, we present a method to account for the circulation-induced magnetic field during geomagnetic field modeling. First, a forward model of the circulation-induced magnetic field is constructed by numerically solving electromagnetic induction equations based on a realistic ocean circulation model. Then, this forward model is subtracted from the observed data. Finally, the core and lithospheric fields, magnetospheric and Earth's mantle-induced fields, and the ocean tide-induced magnetic field are co-estimated. Applying our method to over 20 years of MSS-1, *Swarm*, CryoSat-2, and CHAMP satellite magnetic data, we derive a new multisource geomagnetic field model (MGFM). We find that incorporating a forward model of the circulation-induced magnetic field marginally improves the fit to the data. Furthermore, we demonstrate that neglecting the circulation-induced magnetic field in geomagnetic field modeling results in leakage into the core field model. The highlights of the MGFM model include: (i) a good agreement with the widely used CHAOS model series; (ii) the incorporation of magnetic fields induced by both ocean tides and circulation; and (iii) the suppression of leakage of the circulation-induced magnetic field into the core field model.

Keywords: Macau Science Satellite-1 (MSS-1); geomagnetic field modeling; ocean tides; ocean circulation

1. Introduction

Dedicated geomagnetic satellites like CHAMP (Reigber et al., 2002) and *Swarm* (Friis-Christensen et al., 2006) can measure high-precision and globally covered Earth's magnetic field. Earth's magnetic field measurements contain contributions primarily from the core, lithosphere, and current systems in the ionosphere and magnetosphere. High-precision satellite magnetic data have facilitated the development of numerous geomagnetic field models such as CHAOS (Finlay et al., 2020), CM (Sabaka et al., 2020), POMME (Maus et al., 2010), and GRIMM (Lesur et al., 2015). These models provide significant insights into the structures and dynamics of the Earth's interior (Purucker et al., 2002; Olsen and Mandea, 2008; Lesur et al., 2022; Li JF et al., 2024) and are crucial for geomagnetic heading and navigation systems (Maus et al., 2012). Inspired by the successful launch of the Macau Science Satellite-1 (MSS-1) on May 21, 2023 (Zhang K, 2023), we aim to develop a new multisource geomagnetic field model using the latest MSS-1 and other satellite magnetic data.

Motion of electrically conducting ocean water in the Earth's main magnetic field also generates a measurable induced magnetic field with an amplitude of about 2 nT at satellite altitudes. There are two types of global ocean-induced magnetic fields: the tide-induced magnetic field, driven by the gravitational forces of the Sun and Moon, and the slowly time-varying circulation-induced magnetic field, driven by wind, temperature, and salinity differences. These magnetic fields carry valuable information about ocean dynamics. Currently, the tide-induced magnetic field has been extracted from satellite magnetic data due to its periodic characteristics (Tyler et al., 2003; Sabaka et al., 2015, 2018; Grayver

First author: H. B. Yao, hongbo.yao@outlook.com
Correspondence to: K. Zhang, K.Zhang@exeter.ac.uk
Received 26 DEC 2024; Accepted 12 FEB 2025.
First Published online 04 MAR 2025.

and Olsen, 2019; Sabaka et al., 2020; Saynisch-Wagner et al., 2021; Grayver et al., 2024; Ren ZY et al., 2025). However, the circulation-induced magnetic field lacks periodic characteristics, making its extraction from satellite data challenging. Although some attempts have been made to monitor it (Hornschild et al., 2022; Finlay et al., 2024), there has been no successful extraction of the circulation-induced magnetic field from real satellite data. Consequently, this field has not been previously estimated or incorporated into geomagnetic field models, potentially causing leakage into the core field model.

In this study, we integrate a forward model of the circulation-induced magnetic field into geomagnetic field modeling. This approach enables us to separate the circulation-induced magnetic field from other internal magnetic fields, thereby improving the accuracy of geomagnetic field models. Subsequently, we develop a new geomagnetic field model that accounts for multiple magnetic sources, utilizing data from MSS-1, *Swarm*, CryoSat-2, and CHAMP satellites. Additionally, we investigate the influence of neglecting circulation-induced magnetic field on geomagnetic field modeling.

2. Data and Method

2.1 Data Selection

We utilized magnetic data from MSS-1 (Zhang K, 2023), *Swarm* (Friis-Christensen et al., 2006), CryoSat-2 (Olsen et al., 2020), and CHAMP (Reigber et al., 2002) satellites. The timespans and the number of data points for each satellite are detailed in Table 1. For vector data, we used pre-aligned vector components in the North-East-Center (NEC) frame as provided in the data product files. All data were downsampled to a 1-minute interval. To select data from geomagnetically quiet times in dark regions, we applied the following criteria (Finlay et al., 2020) to all datasets:

- Data from dark regions where the sun is 10° below the horizon.
- The 3-hour planetary K index $Kp \le 2°$.
- The magnetospheric ring current index RC changes by at most 2 nT/h, i.e., $|dRC/dt| \le 2$ nT/h.
- The merging electric field E_m averaged over the previous 2 hours is no more than 0.8 mV/m, i.e., $E_m \le 0.8$ mV/m.
- The interplanetary magnetic field B_z averaged over the previous 2 hours is positive.
- Vector data were used for quasi-dipole latitudes equatorward of ±55°, while scalar data were used for quasi-dipole latitudes poleward of ±55°.

Table 1. Timespans and the number of vector and scalar data points for different satellites.

Satellite	Timespan	Vector	Scalar
CHAMP	2001.01.01–2010.08.31	529,186	186,730
CryoSat-2	2010.09.01–2013.11.30	114,453	60,246
Swarm Alpha	2013.12.01–2024.10.31	341,502	172,331
Swarm Bravo	2013.12.01–2024.10.31	332,811	166,722
Swarm Charlie	2013.12.01–2024.10.31	341,981	16,596
MSS-1	2023.11.02–2024.10.31	40,327	–
Total	2001.01.01-2024.10.31	1,700,260	602,625

After applying these selection criteria, the total number of vector and scalar data points are 1,700,260 and 602,625, respectively. The stacked histogram of the monthly number of data points and the altitudes of different satellites are shown in Figure 1.

2.2 Constructing Forward Model of the Ocean Circulation-Induced Magnetic Field

The circulation-induced field cannot be separated using the regular geometric spherical harmonic method, as it may be masked by the internal core and lithospheric fields. Therefore, we propose incorporating a forward model of the circulation-induced field into geomagnetic field modeling. This forward model involves predicting the circulation-induced magnetic field by numerically solving Maxwell's equations

$$\nabla \times \boldsymbol{E} = -\mathrm{i}\omega \boldsymbol{B}, \tag{1}$$

$$\frac{1}{\mu_0}\nabla \times \boldsymbol{B} = \sigma \boldsymbol{E} + \boldsymbol{J}_s, \tag{2}$$

where $\boldsymbol{E}$ and $\boldsymbol{B}$ represent the electric and magnetic fields induced by global ocean circulation, μ_0 is the magnetic permeability of free space. $\omega = 2\pi/T$ is the angular frequency with T being the period. To mimic steady ocean flow while ensuring numerical stability, the period was set to a large value of 10^9 seconds (about 32 years). σ is an Earth's conductivity model used to account for electromagnetic induction. We use a 3-D conductivity model that includes a realistic distribution of surface oceans and continents

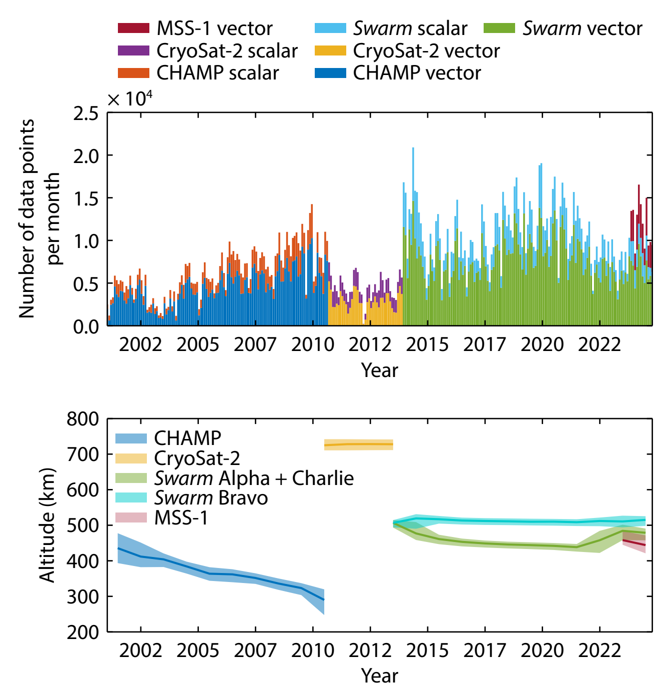

Figure 1. Top: stacked histogram of monthly number of MSS-1, *Swarm*, CryoSat-2, and CHAMP satellite magnetic data points. Bottom: altitude (with respect to a mean geocentric radius of a = 6371.2 km) of different satellites. The lines denote mean altitude while the shaded regions indicate altitude range.

(Yao HB et al., 2022) and an underlying 1-D mantle conductivity model (Grayver et al., 2017). The electric current $\boldsymbol{J}_s$ due to ocean circulation is expressed as (Manoj et al., 2006)

$$\boldsymbol{J}_s = \sigma_{\text{ocean}} (\boldsymbol{v} \times \boldsymbol{B}_{\text{m}}), \tag{3}$$

where σ_{ocean} = 3.2 S/m is the mean seawater conductivity, $\boldsymbol{B}_{\text{m}}$ is the Earth's main magnetic field at the surface estimated from the IGRF-13 magnetic field model (Alken et al., 2021), and $\boldsymbol{v} = \boldsymbol{U}/h$ is the ocean circulation velocity taken from the ECCO ocean circulation model (Forget et al., 2015), where $\boldsymbol{U}$ is the depth-integrated velocity and h the height of the water column. In this study, we consider the primary steady part of the circulation-induced field and ignore the slowly time-varying part. Mean velocity and main field models as averaged from 2001 to 2017 (the latest epoch of the ECCO V4r4 model) are used to obtain the mean electric current. Figure 2 illustrates the eastward and northward components of the depth-integrated velocity averaged over 18 years from the ECCO circulation model. The largest amplitudes of the circulation velocity are located in the region of the Antarctic Circumpolar Current (ACC).

The spherical computational domain is composed of the atmosphere, oceans, and Earth's crust and mantle. The lower boundary is set to the core-mantle boundary, while the upper atmosphere boundary is set to five Earth's radii. To solve the above electromagnetic induction problem, we updated a previously developed finite-element code (Yao HB et al., 2022). The different parts of the forward model are saved to files, including the mesh and the finite-element operator. Thus, without repeatedly solving Maxwell's equations, we can predict rapidly the circulation-induced magnetic field for each given time and location. We should note that the prediction of circulation-induced magnetic signals relies on the velocity model, which can introduce some discrepancies into the model predictions.

Figure 3 presents global maps of the radial circulation-induced magnetic field of the MGFM model at an altitude of 450 km. The predicted amplitude and spatial distribution are in agreement with previous numerical modeling results (Manoj et al., 2006; Šachl et al., 2019). The amplitude of the circulation-induced magnetic field at this altitude is within 2 nT. The largest amplitudes of the magnetic field are found in the region of the ACC. The most prominent feature of the radial circulation-induced magnetic field is a large-scale negative anomaly in the southern Indian Ocean and a positive anomaly in the southern Pacific Ocean, attributed to the significant ocean transports in the ACC region. Additionally, there are smaller magnetic anomalies near Australia.

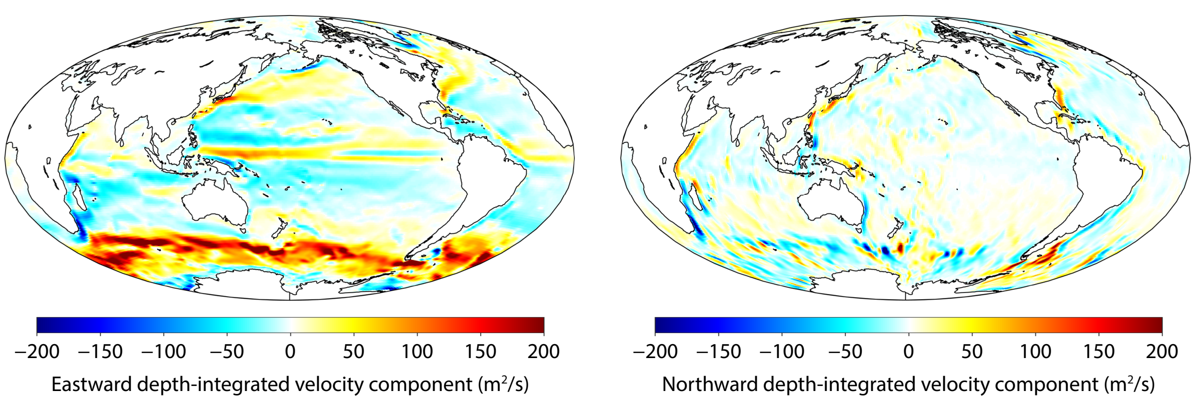

Figure 2. The eastward (left) and northward (right) components of the depth-integrated ocean circulation velocity averaged over 18 years (from 2001 to 2017) of the ECCO model.

2.3 Constructing Core, Lithospheric, Magnetospheric, and Ocean Tide-Induced Magnetic Field Models

The above forward model of the circulation-induced magnetic field was subtracted from observed data. Then, we co-estimate Earth's core, lithospheric, magnetospheric, and tide-induced magnetic fields. In this study, we do not model the ionospheric field but attempt to minimize its contribution through data selection. The magnetic field model $\boldsymbol{B}_{\text{model}}(\boldsymbol{r}, t)$ at location $\boldsymbol{r}$ and time t may be expressed as

$$\boldsymbol{B}_{\text{model}}(\boldsymbol{r}, t) = \boldsymbol{B}_{\text{core}}(\boldsymbol{r}, t) + \boldsymbol{B}_{\text{litho}}(\boldsymbol{r}) + \boldsymbol{B}_{\text{magneto}}(\boldsymbol{r}, t) + \boldsymbol{B}_{\text{tide}}(\boldsymbol{r}, t), \tag{4}$$

where $\boldsymbol{r} = (r, \theta, \phi)$ with r, θ, and ϕ representing the radius, colatitude, and longitude, respectively. $\boldsymbol{B}_{\text{core}}(\boldsymbol{r}, t)$ is the slowly time-varying magnetic field due to the core dynamo. $\boldsymbol{B}_{\text{litho}}(\boldsymbol{r})$ is the static lithospheric magnetic field due to the magnetization of the lithosphere. $\boldsymbol{B}_{\text{magneto}}$ represents the rapidly time-varying magnetic

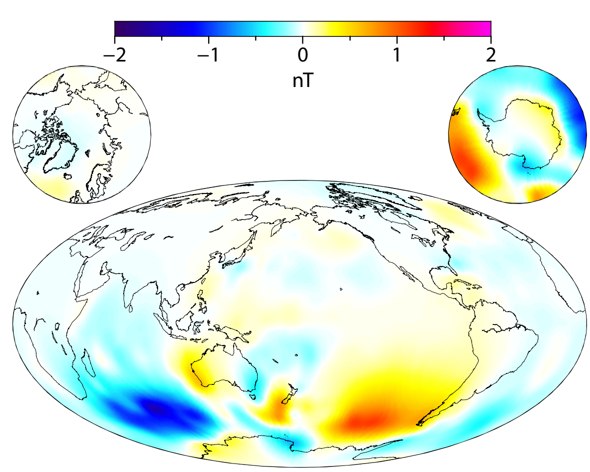

Figure 3. Global map of the radial ocean circulation-induced magnetic field of the MGFM model at 450 km altitude.

fields due to current systems in the magnetosphere and their electromagnetic induction in the Earth's mantle. $\boldsymbol{B}_{\rm tide}(\boldsymbol{r}, t)$ is the time-varying tide-induced magnetic field due to periodic tidal transports (with typical periods of around 12 and 24 hours).

The Earth's mantle-induced magnetic field, resulting from time-varying magnetospheric current systems, depends on the mantle conductivity structure. To produce self-consistent models of Earth's magnetic field and mantle conductivity structure, we have developed a framework for co-estimating the core, lithospheric, and magnetospheric fields, as well as mantle conductivity structure (Yao HB et al., 2025). With this framework, a geomagnetic field model, referred to as the MGFM-alpha model, has also been derived from the MSS-1 and *Swarm* magnetic data. In this study, we extend this framework to incorporate magnetic fields induced by both ocean tides and circulation. The model parametrization for different magnetic sources is described as follows.

2.3.1 Core and lithospheric fields

In source-free regions, the magnetic field $\boldsymbol{B}$ can be written as the negative gradient of a magnetic scalar potential V, i.e. $\boldsymbol{B} = -\nabla V$. This magnetic potential consists of an internal part $V^{\rm int}$ for core and lithospheric fields, an internal part $V^{\rm tide}$ for the tide-induced field, and an external part $V^{\rm ext}$ for magnetospheric and their Earth internal mantle-induced fields. The core and lithospheric field potential $V^{\rm int}$ is described by a spherical harmonic (SH) expansion in the Earth-centered, Earth-fixed (ECEF) geographic coordinate system

$$V^{\rm int}(\boldsymbol{r}, t) = a\sum_{n=1}^{N_{\rm int}}\sum_{m=0}^{n}\left(g_n^m(t)\cos m\phi + h_n^m(t)\sin m\phi\right)\left(\frac{a}{r}\right)^{n+1}P_n^m(\cos\theta), \quad (5)$$

where a = 6371.2 km is the Earth's mean radius, $P_n^m(\cos\theta)$ is the Schmidt quasi-normalized associated Legendre function of degree n and order m (Winch et al., 2005), $N_{\rm int}$ = 80 is the maximum degree used to describe the internal lithospheric field, g_n^m and h_n^m are the model coefficients. Coefficients up to degree $N_{\rm SV}$ = 20 represent the time-dependent core field and are represented by order 6 B-splines (De Boor, 2001) with 6-month knot intervals and fivefold knots at the endpoints, while coefficients for degrees n = 21−80 are time-independent and represent the static lithospheric field.

2.3.2 Magnetospheric and associated induced fields

The magnetic potential $V^{\rm ext}$ for the magnetospheric and induced fields is similar to that used in the CHAOS geomagnetic field model series (Olsen et al., 2006, 2014) and is written as follows

$$\begin{aligned} V^{\rm ext}(\boldsymbol{r}, t) = {} & a\sum_{n=1}^{2}\sum_{m=0}^{n}\left[q_n^{m,\rm SM}(t)\cos m\phi_{\rm SM} + s_n^{m,\rm SM}(t)\sin m\phi_{\rm SM}\right]\left(\frac{r}{a}\right)^{n}P_n^m(\cos\theta_{\rm SM}) \\ & + a\sum_{n=1}^{2}q_n^{0,\rm GSM}\left(\frac{r}{a}\right)^{n}P_n^0(\cos\theta_{\rm GSM}), \end{aligned} \quad (6)$$

where the first part describes the magnetic field due to the magnetospheric ring current in the solar magnetic (SM) coordinate system, the second part describes the magnetic field due to the magnetotail and magnetopause currents in the geocentric solar magnetospheric (GSM) coordinate system; $q_n^{m,\rm SM}$, $s_n^{m,\rm SM}$, and $q_n^{0,\rm GSM}$ represent external model coefficients. The time variability of the model coefficients is a linear function of the *RC* index (Olsen et al., 2014). The Earth's mantle-induced magnetic field is considered by solving Maxwell's equations for a given conductivity model. For more details, interested readers are referred to Yao HB et al. (2025).

2.3.3 Ocean tide-induced field

The tide-induced magnetic field is internal to the satellite measurements. Due to its periodicity, the magnetic potential can be described in the ECEF geographic coordinate system by (Sabaka et al., 2015)

$$V^{\rm tide}(\boldsymbol{r}, t) = {\rm Re}\left[e^{i\omega t}a\sum_{n=1}^{N_{\rm tide}}\sum_{m=-n}^{n}\tau_n^m\left(\frac{a}{r}\right)^{n+1}P_n^{|m|}(\cos\theta)e^{im\phi}\right], \quad (7)$$

where the Re operator takes the real part, τ_n^m represents the complex-valued model coefficients, and $N_{\rm tide}$ = 15 is the maximum degree used to describe the large-scale tide-induced magnetic field. The angular frequency of a specific tidal component is denoted by ω. In this study, we co-estimate the M_2 tidal magnetic field with $\omega = 2\pi/12.42060122$ rad/h. Future studies using along-track and cross-track magnetic gradient data will enable the extraction of signals with a higher spatial resolution (higher cutoff degree $N_{\rm tide}$) and additional tidal components (Sabaka et al., 2016; Grayver and Olsen, 2019; Grayver et al., 2024).

2.3.4 Model estimation

Given the observed magnetic data, we estimate a geomagnetic field model by minimizing the following objective function (Olsen et al., 2014)

$$\phi(\boldsymbol{m}) = \boldsymbol{e}^{\rm T}\boldsymbol{C}_d^{-1}\boldsymbol{e} + \lambda_3\boldsymbol{m}^{\rm T}\boldsymbol{\Lambda}_3\boldsymbol{m} + \lambda_2\boldsymbol{m}^{\rm T}\boldsymbol{\Lambda}_2\boldsymbol{m}, \quad (8)$$

where $\boldsymbol{m}$ is the model parameter vector describing the coefficients of spherical harmonic expansion, and $\boldsymbol{e} = \boldsymbol{d}^{\rm obs} - \boldsymbol{d}^{\rm mod}$ is the data residual vector, with $\boldsymbol{d}^{\rm obs}$ and $\boldsymbol{d}^{\rm mod}$ denoting the observed magnetic data and model predictions, respectively. The matrix $\boldsymbol{C}_d^{-1}$ is the inverse of the data error covariance matrix, accounting for anisotropic errors due to attitude uncertainty (Holme and Bloxham, 1996). Details of the construction of $\boldsymbol{C}_d^{-1}$ can be found in Olsen (2002) and Kloss et al. (2023). The matrices $\boldsymbol{\Lambda}_3$ and $\boldsymbol{\Lambda}_2$ are block diagonal regularization matrices that constrain the third and second-time derivatives of the core field, respectively. Following the CHAOS modeling approach (Olsen et al., 2014; Finlay et al., 2020), $\boldsymbol{\Lambda}_3$ implements a quadratic measure of the third time derivative of the core radial field integrated over the core surface and throughout the model timespan, while $\boldsymbol{\Lambda}_2$ implements a quadratic measure of the second time derivative of the core radial field integrated over the core surface but only at the model endpoints $t_{\rm start}$ = 2001.0 and $t_{\rm end}$ = 2025.0.

The trade-off parameters λ_3 and λ_2 control the strength of regularization. We tested several values for these parameters and selected λ_3 = 1 (nT yr^{-3})$^{-2}$ and λ_2 = 100 (nT yr^{-2})$^{-2}$. As an example, Figure 4 shows the trade-off curve between data misfit $\boldsymbol{e}^{\mathrm{T}}\boldsymbol{C}_d^{-1}\boldsymbol{e}$ and model roughness $\boldsymbol{m}^{\mathrm{T}}\boldsymbol{\Lambda}_3\boldsymbol{m}$ for λ_2 = 100 (nT yr^{-2})$^{-2}$. It demonstrates that λ_3 = 1 (nT yr^{-3})$^{-2}$ provides a good balance between data misfit and model roughness. To minimize the objective function, we implemented an iteratively reweighted least squares method with Huber weights (Constable, 1988) and Gauss-Newton iteration (Farquharson and Oldenburg, 1998; Olsen, 2002).

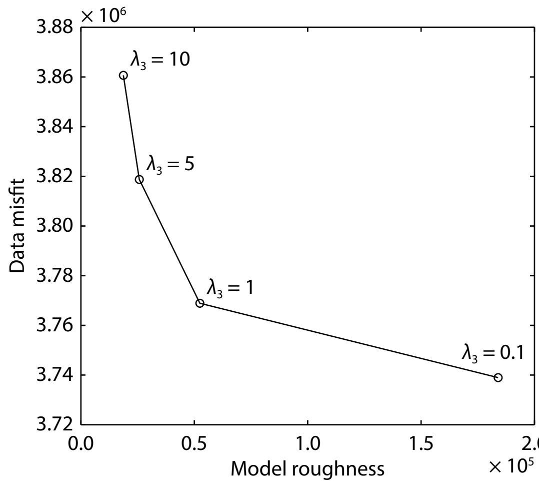

Figure 4. Trade-off curve between data misfit $\boldsymbol{e}^{\mathrm{T}}\boldsymbol{C}_d^{-1}\boldsymbol{e}$ and model roughness $\boldsymbol{m}^{\mathrm{T}}\boldsymbol{\Lambda}_3\boldsymbol{m}$ for λ_2 = 100 (nT yr^{-2})$^{-2}$.

3. Results and Discussion

3.1 Residual Statistics

Table 2 records the number of data points (N_d), Huber-weighted residual mean, and RMS misfit (see Equations (6)–(7) in Olsen et al. (2009) for definitions) at the last iteration of field modeling. For comparison, residual statistics for field modeling with and without incorporating the circulation-induced magnetic field are shown. The residual means for all field components are near zero, and the RMS are comparable with those observed in previous studies (Finlay et al., 2020; Sabaka et al., 2020), indicating a reasonable fit of the geomagnetic field model to the data. The scalar data (F) shows a slightly higher RMS misfit, which is due to the unmodeled polar magnetic fields, such as those caused by the field-aligned current. Including the polar current field in the model would reduce the RMS misfit in polar regions. Despite the circulation-induced magnetic field being weak (about 2 nT at satellite altitudes, which is very small compared to 20,000–60,000 nT of the core field), incorporating it into the geomagnetic field model reduces the data misfit $\boldsymbol{e}^{\mathrm{T}}\boldsymbol{C}_d^{-1}\boldsymbol{e}$ by approximately 0.04%.

3.2 Core Field

The core field dominates on large spatial scales and exhibits secular variations (SV). We evaluate our core field model by comparing its temporal and spatial structures with previous models. Figure 5 shows our core field SH coefficients from 2001.5 to 2024.5 derived with different regularization parameters and the comparison with the widely used CHAOS-7 model (Finlay et al., 2020). Our model's coefficients agree well with the CHAOS-7 model, particularly for low SH-degree coefficients.

Table 2. Number of data points (N_d), Huber-weighted residual mean, and RMS misfit for geomagnetic field modeling with and without incorporating ocean circulation-induced magnetic field.

Satellite	Component	N_d	Without circulation		With circulation	
			Mean	RMS	Mean	RMS
All	F	602,625	0.04	3.91	0.01	3.91
	B_r	1,700,260	0.01	2.80	0.01	2.80
	B_θ	1,700,260	−0.04	3.35	−0.04	3.35
	B_ϕ	1,700,260	−0.06	2.51	−0.06	2.51
CHAMP	F	186,730	−0.07	4.85	−0.10	4.85
	B_r	529,186	−0.08	4.03	−0.08	4.03
	B_θ	529,186	−0.09	4.61	−0.10	4.61
	B_ϕ	529,186	−0.07	2.96	−0.07	2.96
CryoSat-2	F	60,246	0.34	4.50	0.32	4.50
	B_r	114,453	−0.34	3.78	−0.33	3.78
	B_θ	114,453	−0.27	3.76	−0.28	3.76
	B_ϕ	114,453	−0.08	3.21	−0.08	3.20
Swarm Alpha	F	172,331	−0.04	3.35	−0.08	3.35
	B_r	341,502	0.12	1.70	0.12	1.70
	B_θ	341,502	0.06	2.40	0.06	2.40
	B_ϕ	341,502	0.05	2.08	0.05	2.08
Swarm Bravo	F	166,722	0.12	3.10	0.10	3.10
	B_r	332,811	−0.00	1.68	−0.01	1.68
	B_θ	332,811	−0.04	2.40	−0.05	2.40
	B_ϕ	332,811	0.03	2.15	0.03	2.15
Swarm Charlie	F	16,596	−0.08	2.82	−0.11	2.82
	B_r	341,981	0.15	1.74	0.15	1.74
	B_θ	341,981	−0.02	2.42	−0.03	2.42
	B_ϕ	341,981	−0.23	2.15	−0.24	2.15
MSS-1	B_r	40,327	0.07	2.29	0.06	2.29
	B_θ	40,327	0.40	3.10	0.40	3.10
	B_ϕ	40,327	0.00	2.81	0.00	2.81

Figure 6 illustrates the time dependence of the SV field SH coefficients. Since the time derivative of the core field is explicitly constrained during modeling, the SV field coefficients' temporal changes are distinctly influenced by different regularization parameters. Smaller regularization parameters result in more oscillations in model coefficients, such as in the zonal coefficients $\mathrm{d}g_1^0/\mathrm{d}t$ and $\mathrm{d}g_4^0/\mathrm{d}t$, and the sectoral coefficient $\mathrm{d}g_7^7/\mathrm{d}t$. Conversely, larger regularization parameters produce overly smooth temporal changes in the SV field coefficients. We find that λ_3 = 1 (nT yr^{-3})$^{-2}$ strikes a good balance between data misfit and model roughness.

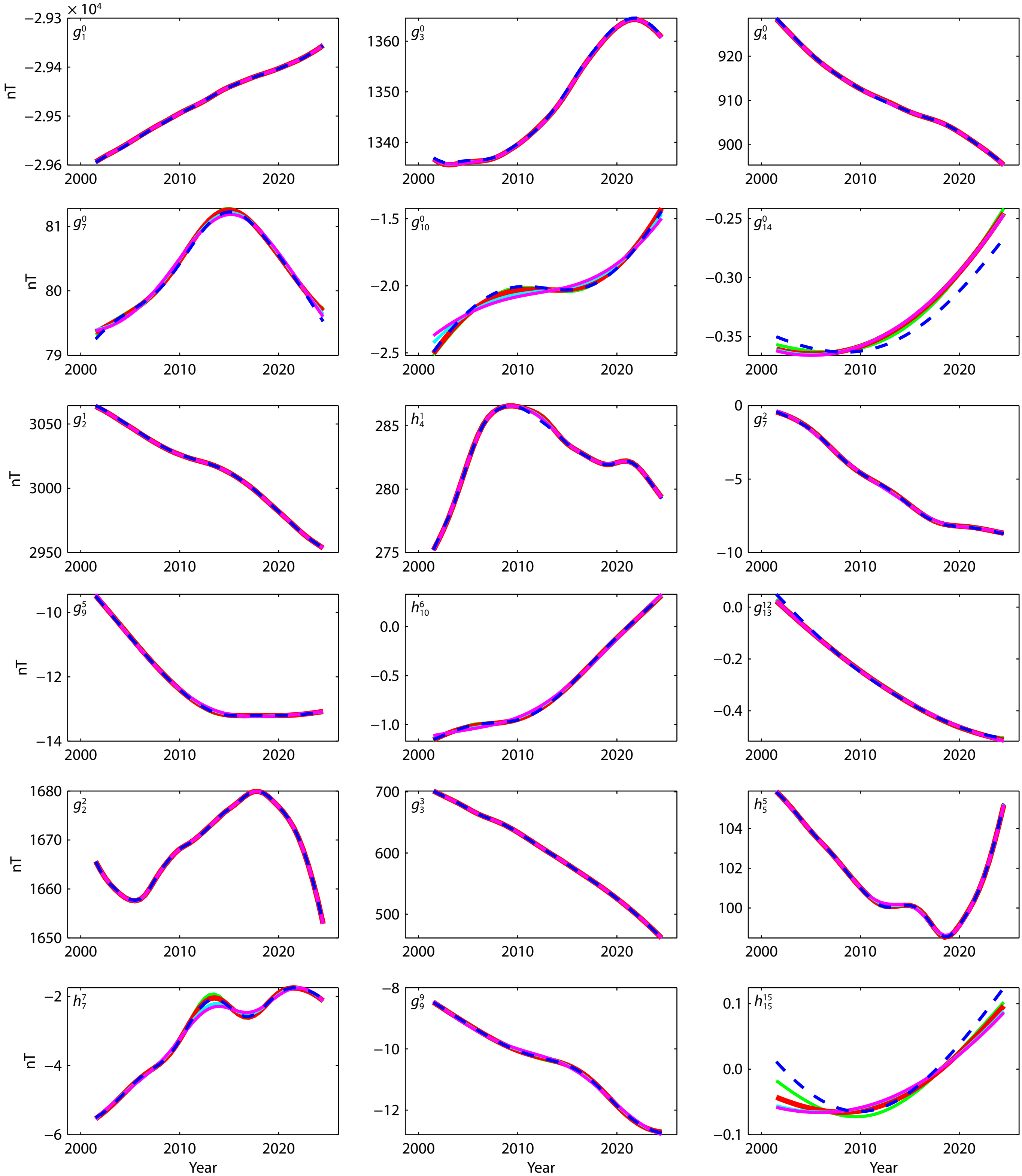

Figure 5. Time-dependence of SH coefficients for the core field from 2001.5 to 2024.5. The top two rows are zonal coefficients, the middle two rows are tesseral coefficients, and the bottom two rows are sectoral coefficients. Models of this study derived with different regularization parameters are shown in green line (λ_3 = 0.1), red line (λ_3 = 1, our preferred model), cyan line (λ_3 = 5), and magenta line (λ_3 = 10). For reference, the CHAOS-7 model is shown in blue dashed line.

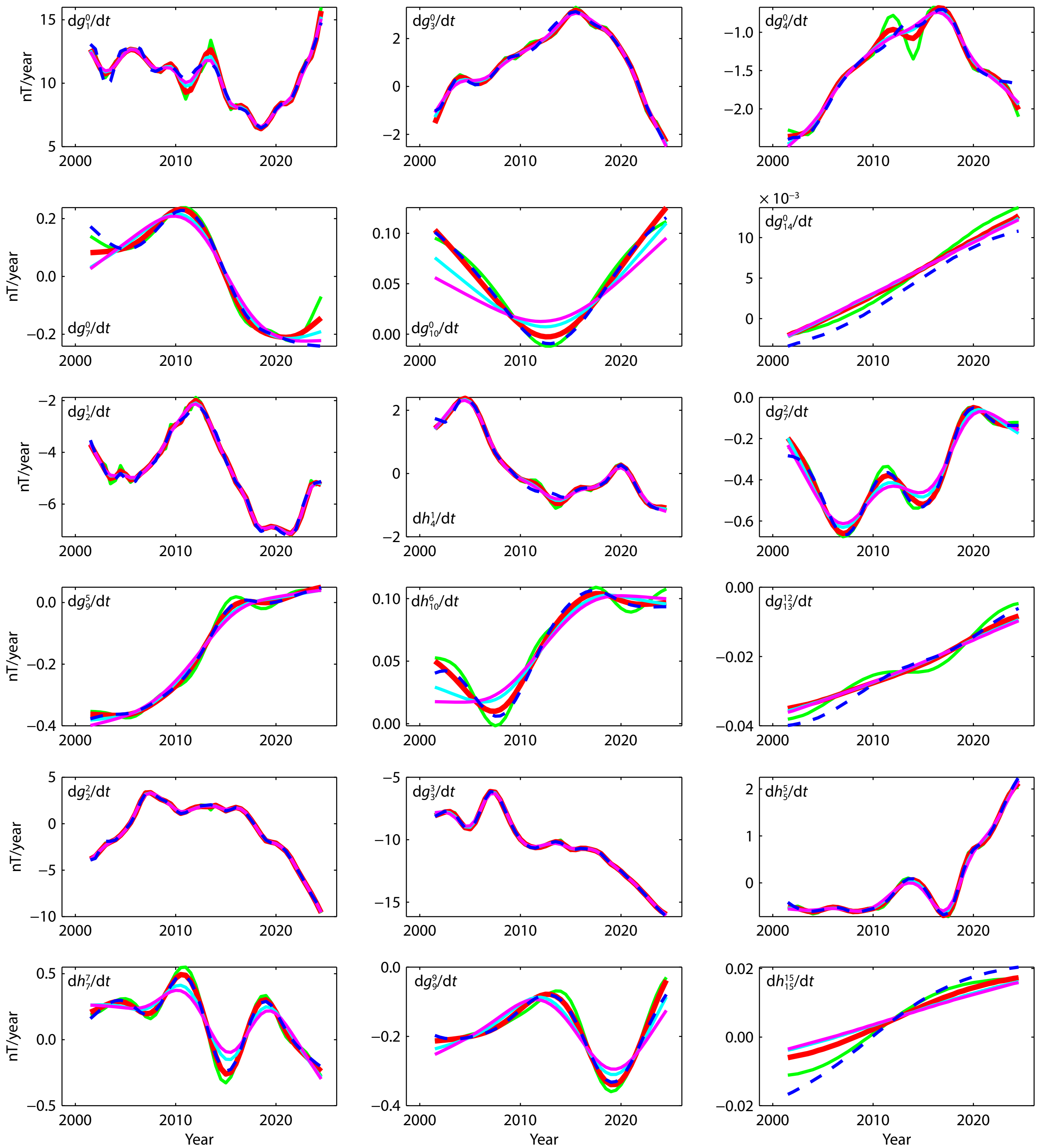

Figure 6. Time-dependence of SH coefficients for the core secular variation from 2001.5 to 2024.5. The top two rows are zonal coefficients, the middle two rows are tesseral coefficients, and the bottom two rows are sectoral coefficients. Models of this study derived with different regularization parameters are shown in green line (λ_3 = 0.1), red line (λ_3 = 1, our preferred model), cyan line (λ_3 = 5), and magenta line (λ_3 = 10). For reference, the CHAOS-7 model is shown in blue dashed line.

This model, referred to as the MGFM core field model (red line in Figure 6), was selected as our preferred model. The main difference between our model and the CHAOS-7 model is smoother variation in high SH degree coefficients in our results. This difference is due to the relaxed temporal regularization applied at higher SH degrees in the CHAOS-7 model. Overall, there is a good agreement between the MGFM and CHAOS-7 SV field time-dependence.

Figure 7 displays the spherical harmonic spectra of the core field

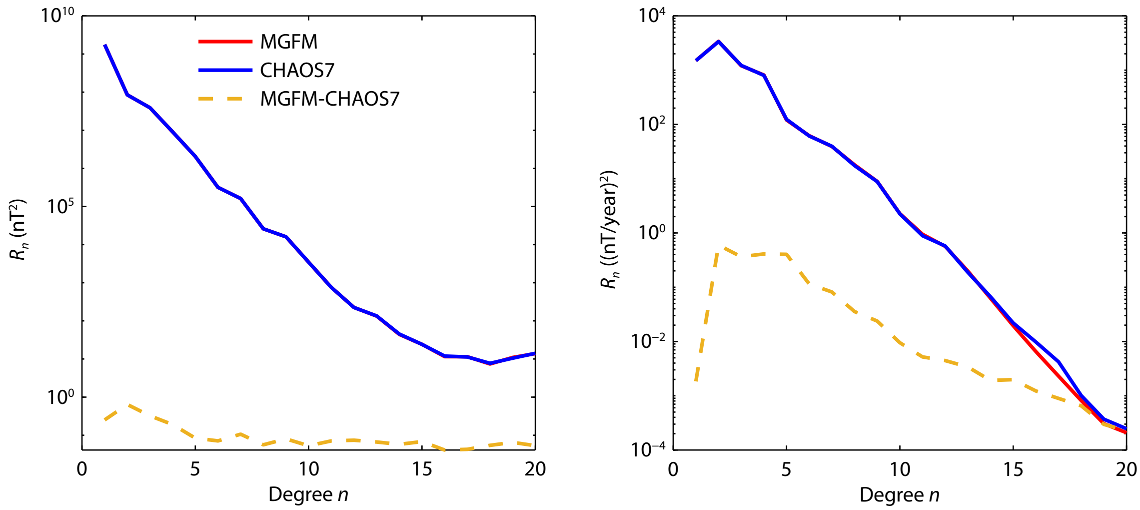

Figure 7. Spherical harmonic spectra of the core field (left) and the secular variation field (right) at the Earth's surface and epoch t = 2024.0 for the MGFM model, CHAOS-7 model, and model difference.

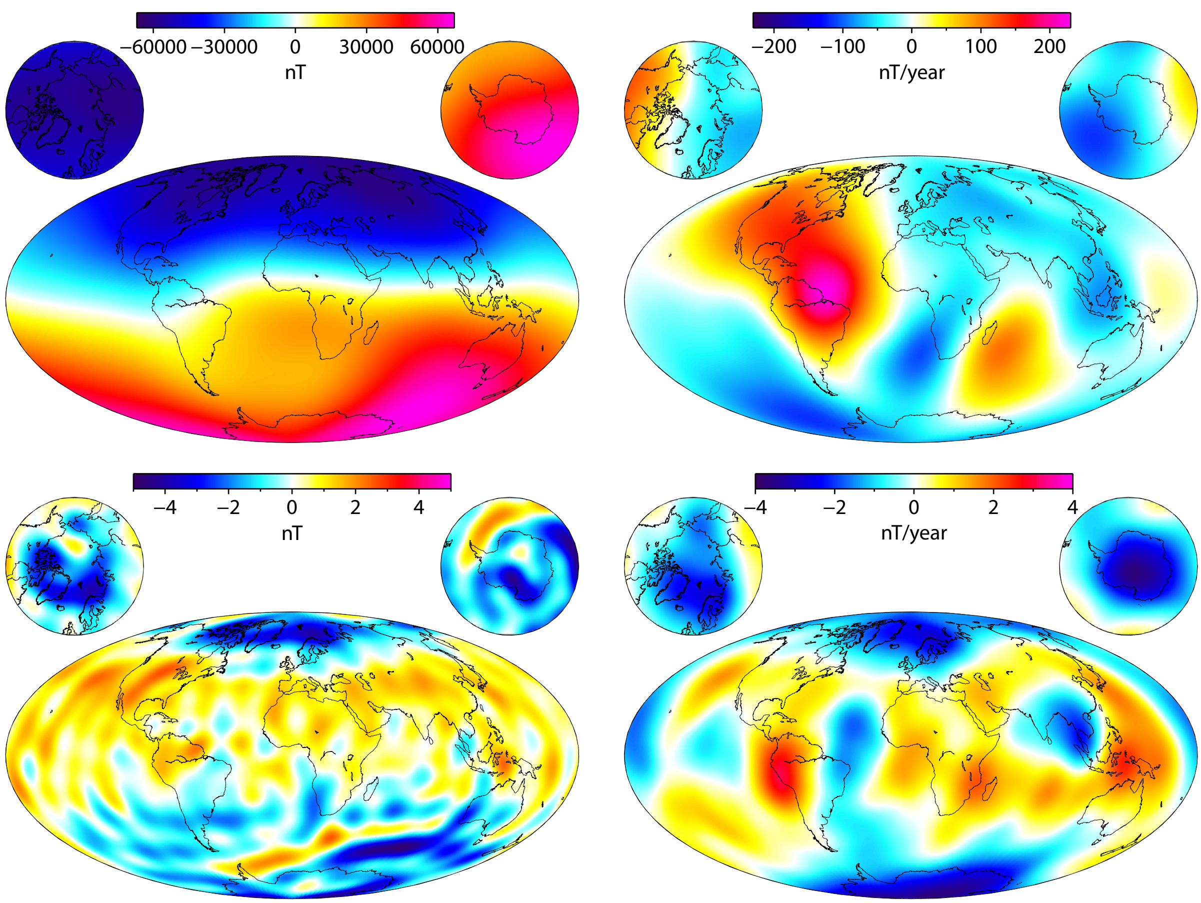

Figure 8. Top: global maps of the radial core magnetic field (left) and the radial secular variation field (right) of the MGFM model at the Earth's surface and epoch t = 2024.0, up to SH degree n = 20. Bottom: radial core field differences (left) and the radial secular variation field differences (right) between the MGFM and CHAOS-7 magnetic field models.

and the SV field at the Earth's surface for epoch t = 2024.0 for the MGFM model, the CHAOS-7 model and model difference. Both the core and SV fields show good agreement, with overall spectral differences below 1 nT^2 and 1 (nT/year)^2 across all SH degrees. The largest discrepancies occur at low SH degrees, likely due to (i) minor differences in handling magnetospheric and associated induced fields (Yao HB et al., 2025), and (ii) the use of different satellite data during the MSS-1 timespan.

The top panel of Figure 8 presents global maps of the radial core magnetic field and the radial SV field of the MGFM model at the

Earth's surface for epoch t = 2024.0, up to SH degree n = 20. The MGFM model successfully captures key features of the core field evaluated on Earth's surface, such as high-latitude patches and the weak field in the South Atlantic. It also represents significant features of the core SV field on the Earth's surface, including the large SV in the northeast corner of South America, the contrasting SV fields in the west and east of South Africa, and a notable negative anomaly in the southeast Pacific and South America. The bottom panel of Figure 8 shows differences between the MGFM and CHAOS-7 magnetic field models. These differences are within ±5 nT for the core field and ±4 nT/year for the SV field, both below 0.02% of the MGFM field values. In summary, our core and SV field models exhibit excellent agreement with the widely used CHAOS-7 model in both temporal and spatial structures.

3.3 Lithospheric Field

Figure 9a shows the spherical harmonic spectra of the lithospheric field at the Earth's surface for various models, along with the spectra differences between our MGFM model, MF7 (Maus et al., 2008), and LCS-1 (Olsen et al., 2017). Note that MF7 and LCS-1 were derived using different modeling techniques and datasets. LCS-1 was entirely derived from CHAMP and *Swarm* magnetic gradient data using an equivalent source method (Kother et al., 2015; Olsen et al., 2017), while MF7 was derived from CHAMP magnetic data using specific pre-processing techniques such as along-track filtering and line leveling (Maus et al., 2008).

Despite these differences, our model shows very good agreement with the published models up to SH degree n = 70. The corresponding degree correlation, as shown in Figure 9b, is greater than 0.9. For SH degrees n = 71−80, the degree correlation remains above 0.85. Our model aligns more closely with the LCS-1 model than with the MF7 model. The sensitivity matrix (normalized coefficient differences in percent), shown in Figures 9c–d, provides a detailed view of coefficient differences, which mainly

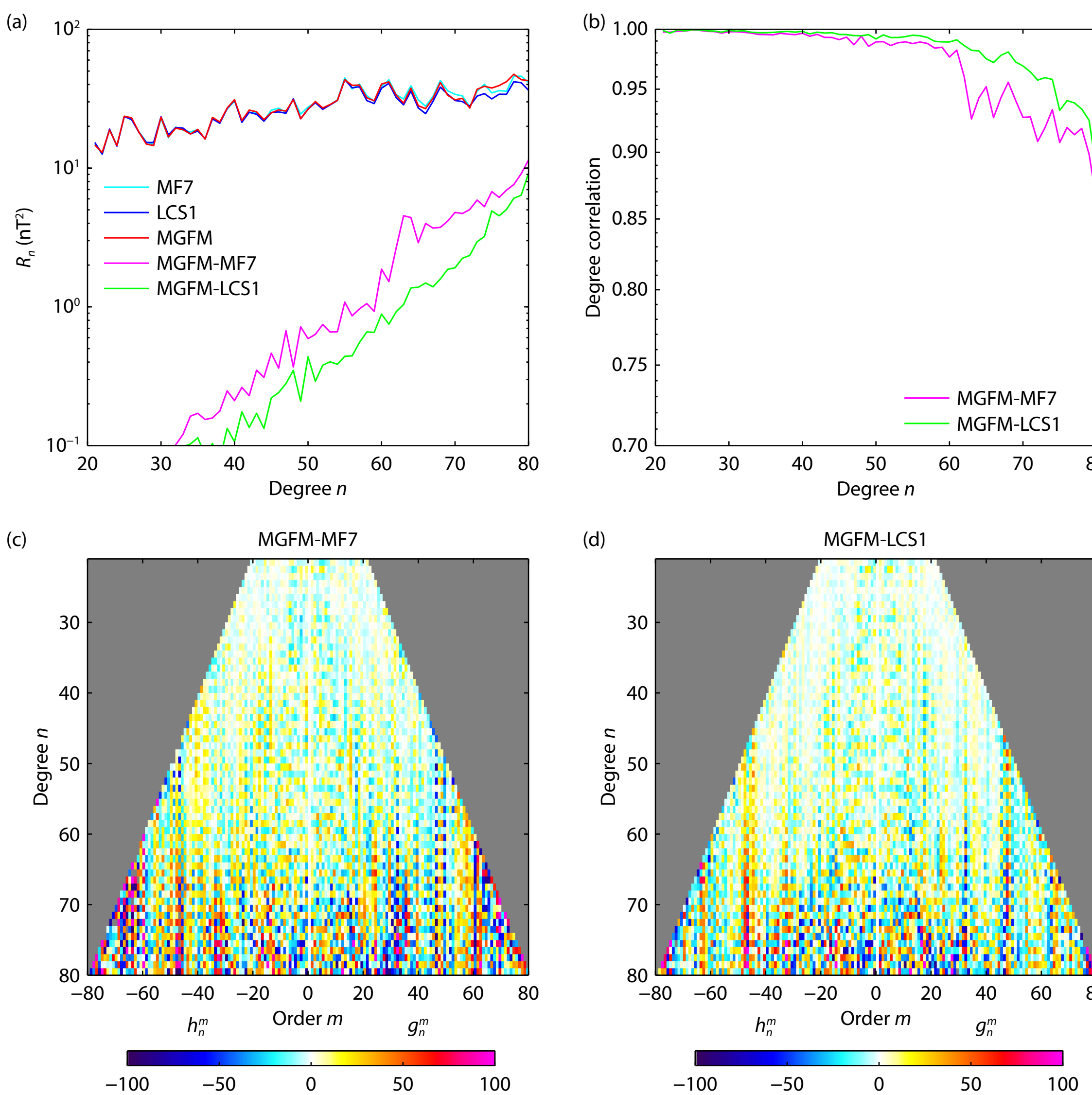

Figure 9. (a) Top left: spherical harmonic spectra of the lithospheric field at the Earth's surface for MF7, LCS-1, and MGFM models and the spectra differences for various models. (b) Top right: degree correlation between various model pairs. (c) Bottom left: sensitivity matrix (normalized coefficient differences in percent) between MGFM and MF7 models. (d) Bottom right: sensitivity matrix between MGFM and LCS-1 models.

occur at high SH degrees. These figures also demonstrate better agreement between MGFM and LCS-1 compared to MF7, likely due to the pre-processing techniques used by MF7 that are not employed in our model or LCS-1, and also due to the use of different data. These results indicate that our model reliably estimates the lithospheric field, at least up to SH degree n = 70.

The top panel of Figure 10 displays the global map of the radial lithospheric magnetic field of the MGFM model at the Earth's surface, calculated from coefficients of degrees n = 21−80. The bottom panel shows differences between the MGFM model and the LCS-1 model. These differences are minor at middle and low latitudes but become more pronounced at high latitudes, especially in regions near Antarctica. This finding is consistent with Olsen et al. (2014), which compared the CHAOS-4 lithospheric field with MF7. The reason for the large difference near Antarctica is not clear; it could be caused by regularization or external magnetic field perturbations. The largest difference at high latitudes is about 58 nT, which is lower than the maximum difference of 75 nT between the CHAOS-4 lithospheric field and MF7 (Olsen et al., 2014). As shown in the top panel, our model successfully reconstructs many magnetic anomalies, including the Bangui anomaly in central Africa.

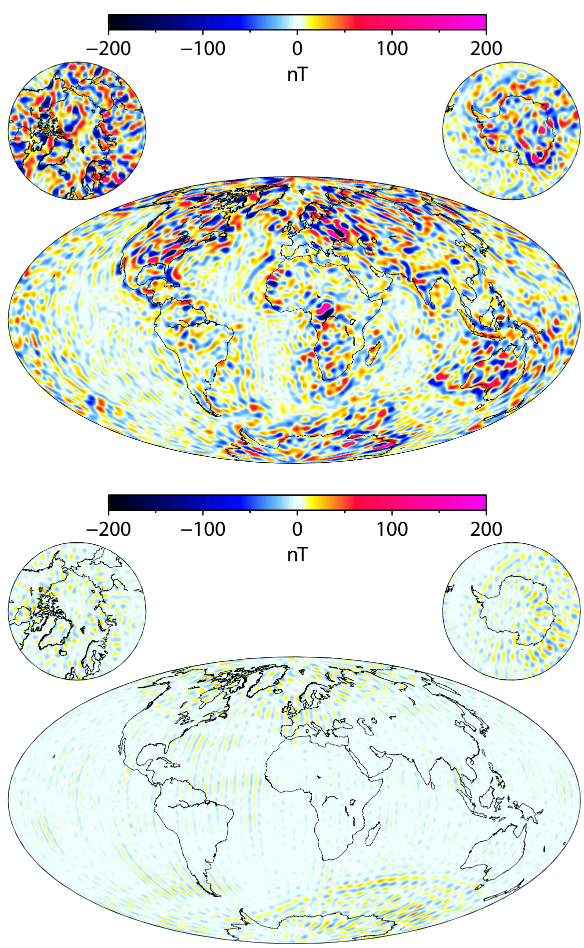

Figure 10. Top: global map of the radial lithospheric magnetic field of the MGFM model at the Earth's surface calculated from coefficients of degrees n = 21−80. Bottom: radial lithospheric field differences between the MGFM and LCS-1 magnetic field models.

3.4 Magnetospheric and Associated Induced Fields

To evaluate the MGFM magnetospheric field model, we predicted the time series of the radial magnetospheric and associated induced fields at four different locations and an altitude of 450 km, using both the MGFM and CHAOS-7 (Finlay et al., 2020) models. The results are presented in Figure 11. For comparison, the Disturbance Storm-Time (*Dst*) index (https://wdc.kugi.kyoto-u.ac.jp/dstdir/), which is derived from ground observatory data and monitors the strength of the magnetospheric ring current, is also shown in the top panel.

Our model predictions align well with those of the CHAOS-7 model across different locations, with differences being close to zero. Notably, the *Dst* index shows a sharp decrease on May 11, 2024, reaching a peak of −412 nT, corresponding to a significant geomagnetic storm on that date (Yan Q and Yao HB, 2024). Both the MGFM and CHAOS-7 models exhibit distinct peaks on May 11, 2024, indicating that the MGFM model successfully captures the key characteristics of the magnetospheric disturbance magnetic field.

3.5 Ocean Tide-Induced Field

Figure 12 shows the real and imaginary parts of the radial component of the M_2 tide-induced magnetic field at a 450 km satellite altitude for various models. The amplitude of this field at 450 km altitude is within 2 nT, consistent with the findings of Grayver and Olsen (2019) and the CM6 model (Sabaka et al., 2020). The field is nearly zero over continents and primarily distributed over oceans, reflecting its oceanic origin. The real part of the radial tide-induced magnetic field is characterized by large-scale structures, such as a significant negative anomaly in the Indian Ocean, and surrounding positive and negative anomalies in eastern and southeastern Australia, as well as several anomalies in the Pacific Ocean. Similarly, the imaginary part is dominated by large-scale structures in the Indian and Pacific Oceans. These features are well captured by the MGFM model, demonstrating that we have effectively extracted the M_2 tide-induced magnetic field from MSS-1, *Swarm*, CryoSat-2, and CHAMP multi-satellite magnetic data.

3.6 Discussion

3.6.1 Influence of neglecting ocean circulation-induced magnetic field

The results shown in Figure 3 indicate that high-precision geomagnetic satellites like MSS-1 and *Swarm* can detect large-scale circulation-induced magnetic field. However, similar to the core field, the circulation-induced magnetic field is internal to the satellite measurements, making it challenging to separate these signals from the core field using potential field modeling methods. Consequently, the large-scale circulation-induced magnetic field could potentially leak into the core field.

In contrast to previous comprehensive (or combined) geomagnetic field modeling approaches such as CHAOS (Olsen et al., 2006; Finlay et al., 2020), CM (Sabaka et al., 2004, 2020), POMME (Maus et al., 2006, 2010), and GRIMM (Lesur et al., 2008, 2015), we incorporated a forward model of the circulation-induced magnetic field into the MGFM model. This was achieved by numerically

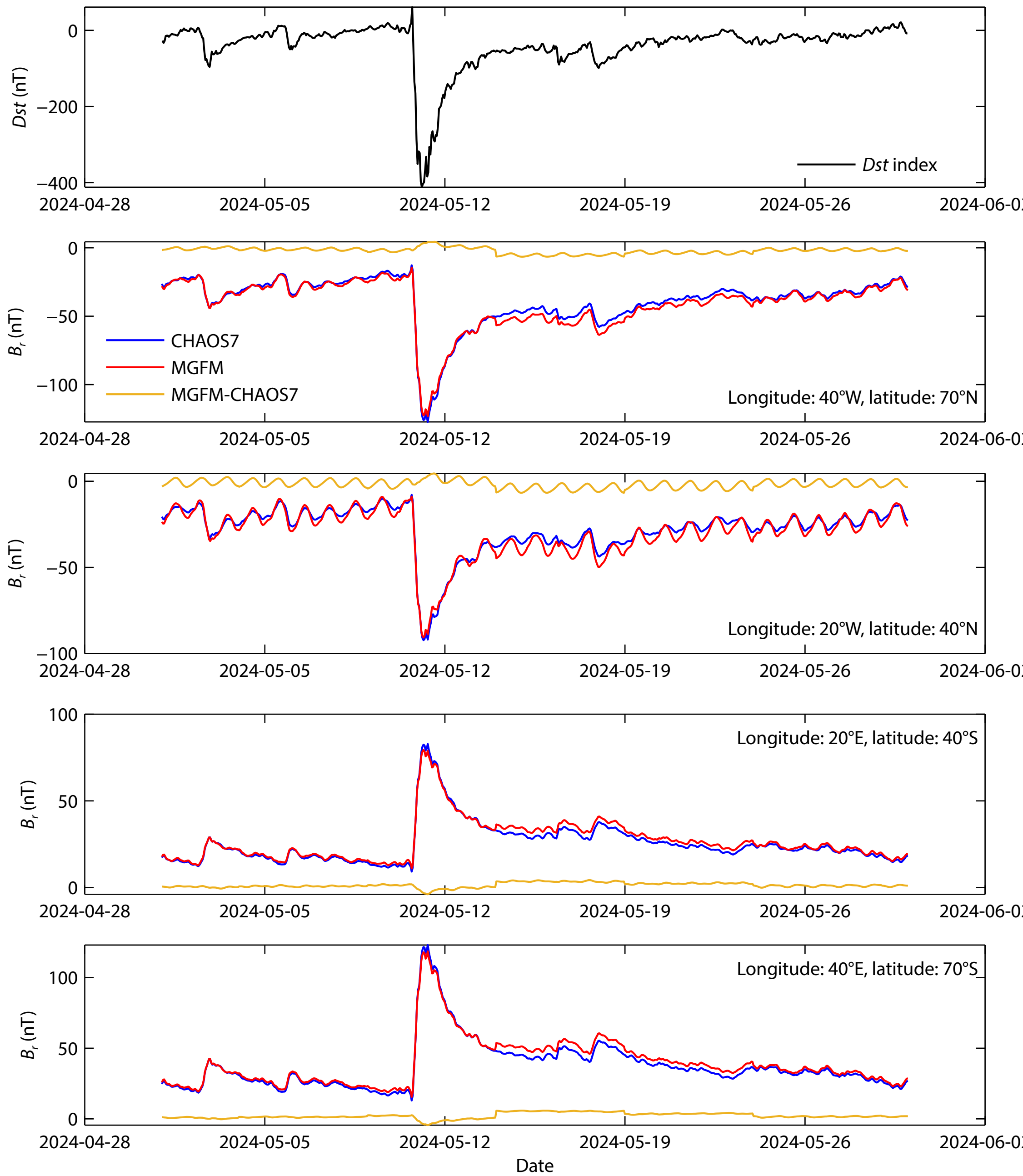

Figure 11. Time series of the *Dst* index (top) followed by the radial magnetospheric magnetic field at four different locations and 450 km altitude predicted by the MGFM and CHAOS-7 magnetic field models.

solving the electromagnetic induction equations excited by the circulation-induced current using a finite-element solver (Yao HB et al., 2022). To assess the impact of neglecting the circulation-induced magnetic field on the estimated core field model, we also performed geomagnetic field modeling without incorporating the circulation-induced magnetic field.

Figure 13 shows the global map of the radial core field differences at 450 km altitude and epoch t = 2024.0 between models with and without incorporating circulation-induced magnetic field. The amplitude of the core field difference aligns with that of the circulation-induced magnetic field as shown in Figure 3. Importantly, the spatial distribution of the core field difference closely matches that of the circulation-induced magnetic field. The only notable discrepancy is that the negative anomaly in the southern Indian Ocean is smaller in scale, while the positive anomaly in the southeastern Indian Ocean is larger. This discrepancy likely relates to the significant core field anomaly in the southeastern Indian Ocean (see the top left panel of Figure 8). These results suggest that previous core field models like the widely used IGRF model (Alken et al., 2021), which were derived without accounting for the circulation-induced magnetic field, also include a small contribution from this field. The strong correlation between Figure 3 and Figure 13 and the reduced data misfit demonstrate that incorporating the physics of equations into geomagnetic field modeling effectively suppresses the leakage of the circulation-induced magnetic field into the core field model.

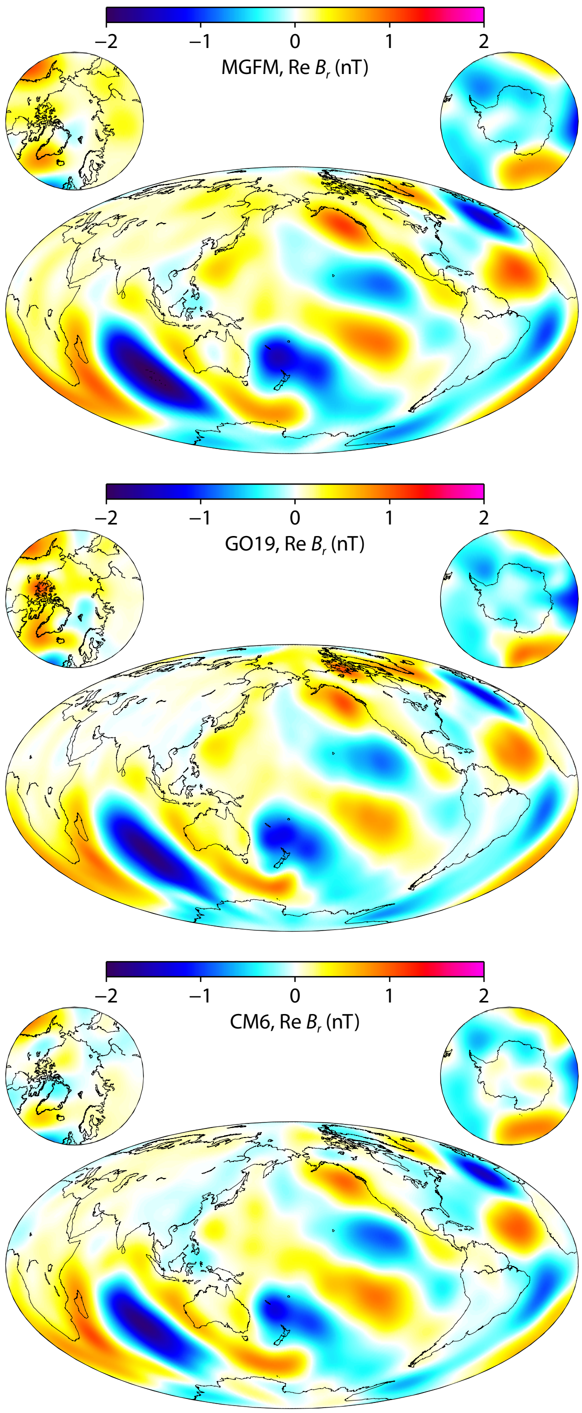

Figure 12. Real (left) and imaginary (right) parts of the radial component (B_r) of the M_2 oceanic tidal magnetic field at 450 km satellite altitude from this study (top), Grayver and Olsen (2019) (middle, denoted as GO19), and the CM6 model (bottom) (Sabaka et al., 2020).

3.6.2 Influence of annual and seasonal variations of ocean circulation model

The electric current generated by ocean circulation depends on oceanic electrical conductivity, circulation velocity, and the main magnetic field (see Equation (3)), with circulation velocity being the dominant factor. We used a mean ocean conductivity value of 3.2 S/m to compute the circulation-induced magnetic field. Previous studies (Grayver et al., 2016) have shown that the impact of seasonal and spatial variations in ocean conductivity on the tide-induced magnetic field is small, with differences due to lateral conductivity variations being less than 0.3 nT at satellite altitude, and those due to seasonal variations being less than 0.03 nT. Thus, using a mean ocean conductivity is also a reasonable approach for accounting for the large-scale circulation-induced magnetic field at satellite altitudes.

The circulation-induced magnetic field consists of a steady mean part and a slowly time-varying part. In this study, we accurately constructed the forward model of the steady mean part (primary part) and ignored the slowly time-varying part (perturbation part).

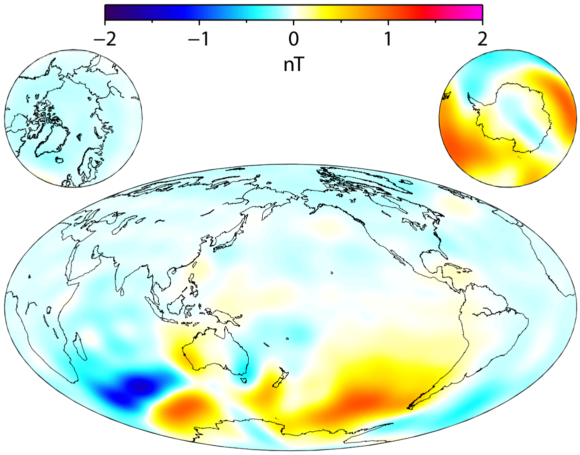

Figure 13. Global map of radial core field differences at 450 km altitude and epoch t = 2024.0 between models with and without incorporating ocean circulation-induced magnetic field.

The mean circulation velocity and main magnetic field were obtained by averaging 18 years of the ECCO circulation velocity model and the IGRF main field model. It has been found (Manoj et al., 2006) that the circulation-induced field difference caused by annual variations in the ocean circulation model is within 0.5 nT, and that caused by seasonal variations is within 0.2 nT. Therefore, considering only the primary mean part is a reasonable first-order approximation.

Nevertheless, it is important to note that annual and seasonal variations in the ocean circulation model may have a small influence on the estimated magnetic field model. For higher accuracy, our method can be extended to account for these variations, although this would require more computational resources to solve the electromagnetic equations for annually and seasonally varied electric currents.

4. Conclusions

We have developed a method to integrate the ocean circulation-induced magnetic field into geomagnetic field modeling. Our framework co-estimates the core and lithospheric fields, the magnetospheric and associated Earth's mantle-induced fields, and the ocean tide-induced magnetic field. A realistic forward model was employed to account for the circulation-induced magnetic field. Using this method, we constructed the first version of the multisource geomagnetic field model (MGFM) based on over 20 years of continuous satellite magnetic data from MSS-1, *Swarm*, CryoSat-2, and CHAMP. Comparisons with previously published models showed good agreement, demonstrating the reliability of our method and model.

We also examined the impact of neglecting the ocean circulation-induced magnetic field. Our results indicate that excluding this field leads to its leakage into the core field model. Our method effectively suppresses this leakage, thereby enhancing the accuracy of geomagnetic field modeling. In the future, by co-estimating the ionospheric field, our method will produce more comprehensive and accurate geomagnetic field models.

Acknowledgments

This work was supported by the National Natural Science Foundation of China (42250101, 42250102) and the Macao Foundation. MSS-1 data are available at https://mss.must.edu.mo/data.html. *Swarm* and Cryosat-2 data are available at http://swarm-diss.eo.esa.int or ftp://swarm-diss.eo.esa.int. CHAMP data are available at ftp.gfz-potsdam.de. We thank Prof. Phil Livermore and two anonymous reviewers for their valuable comments and suggestions that improved the manuscript. The MGFM model predictions for specific times and locations, including the core and lithospheric fields, magnetospheric and Earth's mantle-induced fields, the ocean tide-induced magnetic field, and the ocean circulation-induced magnetic field, are available upon reasonable request.

References

Alken, P., Thébault, E., Beggan, C. D., Amit, H., Aubert, J., Baerenzung, J., Bondar, T. N., Brown, W. J., Califf, S., … Zhou, B. (2021). International geomagnetic reference field: The thirteenth generation. *Earth, Planets Space*, *73*(1), 49. https://doi.org/10.1186/s40623-020-01288-x

Constable, C. G. (1988). Parameter estimation in non-Gaussian noise. *Geophys. J. Int.*, *94*(1), 131–142. https://doi.org/10.1111/j.1365-246x.1988.tb03433.x

De Boor, C. (2001). *A Practical Guide to Splines*. New York: Springer.

Farquharson, C. G., and Oldenburg, D. W. (1998). Non-linear inversion using general measures of data misfit and model structure. *Geophys. J. Int.*, *134*(1), 213–227. https://doi.org/10.1046/j.1365-246x.1998.00555.x

Finlay, C. C., Kloss, C., Olsen, N., Hammer, M. D., Tøffner-Clausen, L., Grayver, A., and Kuvshinov, A. (2020). The CHAOS-7 geomagnetic field model and observed changes in the South Atlantic Anomaly. *Earth, Planets Space*, *72*(1), 156. https://doi.org/10.1186/s40623-020-01252-9

Finlay, C. C., Velímský, J., Kloss, C., and Blangsbøll, R. M. (2024). Satellite monitoring of long period ocean-induced magnetic field variations. *Phil. Trans. R. Soc. A: Math., Phys. Eng. Sci.*, *382*(2286), 20240077. https://doi.org/10.1098/rsta.2024.0077

Forget, G., Campin, J. M., Heimbach, P., Hill, C. N., Ponte, R. M., and Wunsch, C. (2015). ECCO version 4: An integrated framework for non-linear inverse modeling and global ocean state estimation. *Geosci. Model Dev.*, *8*(10), 3071–3104. https://doi.org/10.5194/gmd-8-3071-2015

Friis-Christensen, E., Lühr, H., and Hulot, G. (2006). *Swarm*: A constellation to study the Earth's magnetic field. *Earth, Planets Space*, *58*(4), 351–358. https://doi.org/10.1186/bf03351933

Grayver, A., Finlay, C. C., and Olsen, N. (2024). Magnetic signals from oceanic tides: New satellite observations and applications. *Phil. Trans. R. Soc. A: Math., Phys. Eng. Sci.*, *382*(2286), 20240078. https://doi.org/10.1098/rsta.2024.0078

Grayver, A. V., Schnepf, N. R., Kuvshinov, A. V., Sabaka, T. J., Manoj, C., and Olsen, N. (2016). Satellite tidal magnetic signals constrain oceanic lithosphere-asthenosphere boundary. *Sci. Adv.*, *2*(9), e1600798. https://doi.org/10.1126/sciadv.1600798

Grayver, A. V., Munch, F. D., Kuvshinov, A. V., Khan, A., Sabaka, T. J., and Tøffner-Clausen, L. (2017). Joint inversion of satellite-detected tidal and magnetospheric signals constrains electrical conductivity and water content of the upper mantle and transition zone. *Geophys. Res. Lett.*, *44*(12), 6074–6081. https://doi.org/10.1002/2017gl073446

Grayver, A. V., and Olsen, N. (2019). The magnetic signatures of the M_2, N_2, and O_1 oceanic tides observed in Swarm and CHAMP satellite magnetic data. *Geophys. Res. Lett.*, *46*(8), 4230–4238. https://doi.org/10.1029/2019gl082400

Holme, R., and Bloxham, J. (1996). The treatment of attitude errors in satellite geomagnetic data. *Phys. Earth Planet. Inter.*, *98*(3-4), 221–233. https://doi.org/10.1016/s0031-9201(96)03189-5

Hornschild, A., Baerenzung, J., Saynisch-Wagner, J., Irrgang, C., and Thomas, M. (2022). On the detectability of the magnetic fields induced by ocean circulation in geomagnetic satellite observations. *Earth, Planets Space*, *74*(1), 182. https://doi.org/10.1186/s40623-022-01741-z

Kloss, C., Finlay, C. C., Laundal, K. M., and Olsen, N. (2023). Polar ionospheric currents and high temporal resolution geomagnetic field models. *Geophys. J. Int.*, *235*(2), 1736–1760. https://doi.org/10.1093/gji/ggad325

Kother, L., Hammer, M. D., Finlay, C. C., and Olsen, N. (2015). An equivalent source method for modelling the global lithospheric magnetic field. *Geophys. J. Int.*, *203*(1), 553–566. https://doi.org/10.1093/gji/ggv317

Lesur, V., Wardinski, I, Rother, M., and Mandea, M. (2008). GRIMM: The GFZ Reference Internal Magnetic Model based on vector satellite and observatory data. *Geophys. J. Int.*, *173*(2), 382–394. https://doi.org/10.1111/j.1365-246x.2008.03724.x

Lesur, V., Whaler, K., and Wardinski, I. (2015). Are geomagnetic data consistent with stably stratified flow at the core–mantle boundary?. *Geophys. J. Int.*, *201*(2), 929–946. https://doi.org/10.1093/gji/ggv031

Lesur, V., Gillet, N., Hammer, M. D., and Mandea, M. (2022). Rapid variations of Earth's core magnetic field. *Surv. Geophys.*, *43*(1), 41–69. https://doi.org/10.1007/s10712-021-09662-4

Li, J. F., Lin, Y. F., and Zhang, K. (2024). Dynamic mode decomposition of the core surface flow inverted from geomagnetic field models. *Geophys. Res. Lett.*, *51*(1), e2023GL106362. https://doi.org/10.1029/2023gl106362

Manoj, C., Kuvshinov, A., Maus, S., and Lühr, H. (2006). Ocean circulation generated magnetic signals. *Earth, Planets Space*, *58*(4), 429–437. https://doi.org/10.1186/bf03351939

Maus, S., Rother, M., Stolle, C., Mai, W., Choi, S., Lühr, H., Cooke, D., and Roth, C. (2006). Third generation of the Potsdam Magnetic Model of the Earth (POMME. *Geochem., Geophys., Geosyst.*, *7*(7), Q07008. https://doi.org/10.1029/2006gc001269

Maus, S., Yin, F., Lühr, H., Manoj, C., Rother, M., Rauberg, J., Michaelis, I., Stolle, C., and Müller, R. D. (2008). Resolution of direction of oceanic magnetic lineations by the sixth-generation lithospheric magnetic field model from CHAMP satellite magnetic measurements. *Geochem., Geophys., Geosyst.*, *9*(7), Q07021. https://doi.org/10.1029/2008gc001949

Maus, S., Manoj, C., Rauberg, J., Michaelis, I., and Lühr, H. (2010). NOAA/NGDC candidate models for the 11th generation International Geomagnetic Reference Field and the concurrent release of the 6th generation POMME magnetic model. *Earth, Planets Space*, *62*(10), 729–735. https://doi.org/10.5047/eps.2010.07.006

Maus, S., Nair, M. C., Poedjono, B., Okewunmi, S., Fairhead, D., Barckhausen, U., Milligan, P. R., and Matzka, J. (2012). High Definition Geomagnetic Models: A new perspective for improved wellbore positioning. In *Proceedings of IADC/SPE Drilling Conference and Exhibition* (pp. SPE-151436-MS). San Diego, USA: SPE. https://doi.org/10.2118/151436-ms

Olsen, N. (2002). A model of the geomagnetic field and its secular variation for epoch 2000 estimated from Ørsted data. *Geophys. J. Int.*, *149*(2), 454–462. https://doi.org/10.1046/j.1365-246x.2002.01657.x

Olsen, N., Lühr, H., Sabaka, T. J., Mandea, M., Rother, M., Tøffner-Clausen, L., and Choi, S. (2006). CHAOS-a model of the Earth's magnetic field derived from CHAMP, Ørsted, and SAC-C magnetic satellite data. *Geophys. J. Int.*, *166*(1), 67–75. https://doi.org/10.1111/j.1365-246x.2006.02959.x

Olsen, N., and Mandea, M. (2008). Rapidly changing flows in the Earth's core. *Nat. Geosci.*, *1*(6), 390–394. https://doi.org/10.1038/ngeo203

Olsen, N., Mandea, M., Sabaka, T. J., and Tøffner-Clausen, L. (2009). CHAOS-2-a geomagnetic field model derived from one decade of continuous satellite data. *Geophys. J. Int.*, *179*(3), 1477–1487. https://doi.org/10.1111/j.1365-246x.2009.04386.x

Olsen, N., Lühr, H., Finlay, C. C., Sabaka, T. J., Michaelis, I., Rauberg, J, and Tøffner-Clausen, L. (2014). The CHAOS-4 geomagnetic field model. *Geophys. J. Int.*, *197*(2), 815–827. https://doi.org/10.1093/gji/ggu033

Olsen, N., Ravat, D., Finlay, C. C., and Kother, L. K. (2017). LCS-1: A high-resolution global model of the lithospheric magnetic field derived from CHAMP and Swarm satellite observations. *Geophys. J. Int.*, *211*(3), 1461–1477. https://doi.org/10.1093/gji/ggx381

Olsen, N., Albini, G., Bouffard, J., Parrinello, T., and Tøffner-Clausen, L. (2020). Magnetic observations from CryoSat-2: Calibration and processing of satellite platform magnetometer data. *Earth, Planets Space*, *72*(1), 48. https://doi.org/10.1186/s40623-020-01171-9

Purucker, M., Langlais, B., Olsen, N., Hulot, G., and Mandea, M. (2002). The southern edge of cratonic North America: Evidence from new satellite magnetometer observations. *Geophys. Res. Lett.*, *29*(15), 8000. https://doi.org/10.1029/2001gl013645

Reigber, C., Lühr, H., and Schwintzer, P. (2002). CHAMP mission status. *Adv. Space Res.*, *30*(2), 129–134. https://doi.org/10.1016/s0273-1177(02)00276-4

Ren, Z. Y., Huang, Y. P., Yang, C., Chen, C. J., and Zhang, K. (2025). Preliminary results suggest observations from Macau Science Satellite-1 system can improve knowledge of tidal-induced magnetic fields. *Earth Planet. Phys.*, *9*(3), 586–594. https://doi.org/10.26464/epp2025002

Sabaka, T. J., Olsen, N., and Purucker, M. E. (2004). Extending comprehensive models of the Earth's magnetic field with Ørsted and CHAMP data. *Geophys. J. Int.*, *159*(2), 521–547. https://doi.org/10.1111/j.1365-246x.2004.02421.x

Sabaka, T. J., Olsen, N., Tyler, R. H., and Kuvshinov, A. (2015). CM5, a pre-Swarm comprehensive geomagnetic field model derived from over 12 yr of CHAMP, Ørsted, SAC-C and observatory data. *Geophys. J. Int.*, *200*(3), 1596–1626. https://doi.org/10.1093/gji/ggu493

Sabaka, T. J., Tyler, R. H., and Olsen, N. (2016). Extracting ocean-generated tidal magnetic signals from Swarm data through satellite gradiometry. *Geophys. Res. Lett.*, *43*(7), 3237–3245. https://doi.org/10.1002/2016gl068180

Sabaka, T. J., Tøffner-Clausen, L., Olsen, N., and Finlay, C. C. (2018). A comprehensive model of Earth's magnetic field determined from 4 years of Swarm satellite observations. *Earth, Planets Space*, *70*(1), 130. https://doi.org/10.1186/s40623-018-0896-3

Sabaka, T. J., Tøffner-Clausen, L., Olsen, N., and Finlay, C. C. (2020). CM6: A comprehensive geomagnetic field model derived from both CHAMP and Swarm satellite observations. *Earth, Planets Space*, *72*(1), 80. https://doi.org/10.1186/s40623-020-01210-5

Šachl, L., Martinec, Z., Velímský, J., Irrgang, C., Petereit, J., Saynisch, J., Einšpigel, D., and Schnepf, N. R. (2019). Modelling of electromagnetic signatures of global ocean circulation: Physical approximations and numerical issues. *Earth, Planets Space*, *71*(1), 58. https://doi.org/10.1186/s40623-019-1033-7

Saynisch-Wagner, J., Baerenzung, J., Hornschild, A., Irrgang, C., and Thomas, M. (2021). Tide-induced magnetic signals and their errors derived from CHAMP and Swarm satellite magnetometer observations. *Earth, Planets Space*, *73*(1), 234. https://doi.org/10.1186/s40623-021-01557-3

Tyler, R. H., Maus, S., and Luhr, H. (2003). Satellite observations of magnetic fields due to ocean tidal flow. *Science*, *299*(5604), 239–241. https://doi.org/10.1126/science.1078074

Winch, D. E., Ivers, D. J., Turner, J. P. R., and Stening, R. J. (2005). Geomagnetism and Schmidt quasi-normalization. *Geophys. J. Int.*, *160*(2), 487–504. https://doi.org/10.1111/j.1365-246x.2004.02472.x

Yan, Q., and Yao, H. B. (2024). Recent geomagnetic storms observed by Macau Science Satellite-1. *Earth Planet. Phys.*, *8*(4), 565–569. https://doi.org/10.26464/epp2024047

Yao, H. B., Ren, Z. Y., Tang, J. T., and Zhang, K. (2022). A multi-resolution finite-element approach for global electromagnetic induction modeling with application to southeast China coastal geomagnetic observatory studies. *J. Geophys. Res.: Solid Earth*, *127*(8), e2022JB024659. https://doi.org/10.1029/2022jb024659

Yao, H. B., Xu, J. Y., and Zhang, K. (2025). A method for simultaneously determining Earth's magnetic field and mantle conductivity models using MSS-1 and Swarm satellite magnetic data. *Phys. Earth Planet. Inter.*, *358*, 107296. https://doi.org/10.1016/j.pepi.2024.107296

Zhang, K. (2023). A novel geomagnetic satellite constellation: Science and applications. *Earth Planet. Phys.*, *7*(1), 4–21. https://doi.org/10.26464/epp2023019